*J. Fluid Mech.* (1980), *vol.* 99, *part* 1, *pp.* 111–127
*Printed in Great Britain*



# Velocity measurements inside a rotating cylindrical cavity with a radial outflow of fluid

By J. M. OWEN AND J. R. PINCOMBE

School of Engineering and Applied Sciences,
University of Sussex, U.K.

(Received 1 June 1979)

Flow visualization and laser-doppler anemometry have been used to determine the flow structure and measure the velocity distribution inside a rotating cylindrical cavity with an outer to inner radius ratio of 10, and an axial spacing to inner radius ratio of 2·67. A flow structure comprising an inner layer, Ekman layers, an outer layer and an interior potential core has been confirmed for the cases where the inlet air enters the cavity either axially, through a central hole, or radially, through a central gauze tube, and leaves radially through a series of holes in the peripheral shroud. Velocity measurements in the laminar Ekman layers agree well with the 'modified linear theory', and long- and short-wavelength disturbances (which have been reported by other experimenters) have been observed on the Ekman layers when the radial Reynolds number exceeds a critical value. The phenomenon of reverse flow in the Ekman layers and the possibility of ingress of external fluid through the holes in the shroud have also been observed.

## 1. Introduction

The rotating cylindrical cavity with a radial outflow of fluid shown in figure 1(*a*) provides a simple model of co-rotating air-cooled gas turbine disks. In the turbine, cooling air enters axially through a central hole, of radius $r = a$, in one disk and exits radially through a series of holes in the shroud at $r = b$. Owen & Bilimoria (1977) have made heat-transfer measurements for a range of rotational Reynolds numbers, $Re_\theta$ ($Re_\theta \equiv \Omega b^2/\nu$), coolant flow rates, $C_w$ $C_w \equiv Q/\nu b$, $Q$ being the volumetric flow rate), and gap ratios, $G(G \equiv s/b)$, for such cavities as well as for cavities with an axial through flow of coolant through a central hole in each disk. In the latter case, measurements were strongly influenced by the occurrence of vortex breakdown in the central axial jet; this phenomenon was studied separately, under isothermal conditions, by Owen & Pincombe (1979). They related the occurrence of spiral and axisymmetric vortex breakdown with the axial Rossby number $\epsilon_z$ ($\epsilon_z \equiv \overline{W}/\Omega a$, where $\overline{W}$ is the bulk-average velocity of the central jet, $\overline{W} = Q/\pi a^2$).

Considerable insight into the structure of laminar flow inside a rotating cavity with a uniform source at $r = a$ and sink at $r = b$, see figure 1(*b*), has been provided by Hide (1968).The flow can be divided into four regions:

(i) an inner layer of thickness $\Delta_E$;

(ii) separate Ekman layers with a thickness of approximately $3D$ ($D \equiv (\nu/\Omega)^{\frac{1}{2}}$), on each disk;

(iii) an outer layer of thickness $\Delta_K$; and

(iv) a potential core in which radial and axial components of velocity are zero.

0022–1120/80/4476–1330 $02.00 

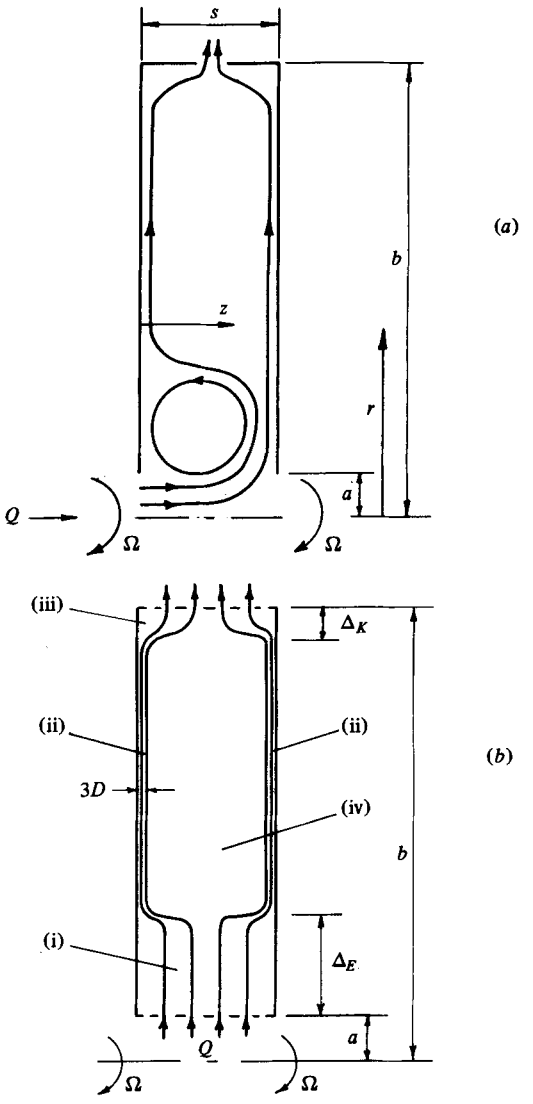


FIGURE 1. Schematic diagram of a rotating cylindrical cavity with a radial outflow. (*a*) Axial inlet; (*b*) radial inlet.

In the tests described below, flow visualization and laser-doppler anemometry are used to determine the flow structure and to measure the velocity distribution in a rotating cavity with an axial inlet; and these results are compared with those obtained for the radial inlet case.

Hide's analysis is limited to laminar flow whereas gas turbines normally operate under turbulent conditions. However, the precise criteria for transition from laminar to turbulent flow inside rotating cavities are still not known. Ekman-layer instability has been investigated by Faller (1963) and Tatro & Mollo-Christensen (1967) for the case of a rotating cylindrical cavity with radial inflow. Two types of instability were observed: type I waves with a wavelength, $\lambda$, of $\lambda/D \simeq 12$; type II waves with $25 < \lambda/D < 33$. The occurrence of these waves depends on the radial Reynolds

number, $Re_r$ ($Re_r \equiv Q/2\Pi\nu r$), and the radial Rossby number, $\epsilon_r$ ($\epsilon_r \equiv Q/4\pi r^2\Omega D$; the radial Rossby number is the ratio of the average radial velocity in the Ekman layer to the tangential velocity of the cavity at the same radial location). As $\epsilon_r \to 0$, Tatro & Mollo-Christensen found that type II waves occur at $Re_r \simeq 56$, and types I and II were both present at $Re_r > 125$. Above this value, the first manifestations of turbulence were observed as bursts of high-frequency fluctuations, but a low-frequency periodic structure was seen at Reynolds numbers well above transition. As Coriolis forces dominate in both the radial inflow and outflow cases, and as the flow structure is similar for both cases, it is probable that the instabilities noted above for inflow should also occur for the outflow case considered below.

In §2, a summary of the salient points of Hide's analysis is presented. In §3 the experimental apparatus is described, and in §§4 and 5 the results obtained by flow visualization and laser-doppler anemometry, respectively, are discussed for the flows illustrated in figure 1.

## 2. Source–sink flow in a rotating fluid

For steady, incompressible, laminar, axisymmetric flow, the Navier–Stokes and continuity equations may be expressed as

$$\left\{u\frac{\partial u}{\partial r}+w\frac{\partial u}{\partial z}-\frac{v^2}{r}\right\}-2\Omega v = -\frac{1}{\rho}\frac{\partial p^1}{\partial r}+\nu\left(\frac{\partial^2 u}{\partial r^2}+\frac{1}{r}\frac{\partial u}{\partial r}-\frac{u}{r^2}+\frac{\partial^2 u}{\partial z^2}\right), \tag{2.1a}$$

$$\left\{u\frac{\partial v}{\partial r}+w\frac{\partial v}{\partial z}+\frac{uv}{r}\right\}+2\Omega u = \nu\left(\frac{\partial^2 v}{\partial r^2}+\frac{1}{r}\frac{\partial v}{\partial r}-\frac{v}{r^2}+\frac{\partial^2 v}{\partial z^2}\right), \tag{2.1b}$$

$$\left\{u\frac{\partial w}{\partial r}+w\frac{\partial w}{\partial z}\right\} = -\frac{1}{\rho}\frac{\partial p}{\partial z}+\nu\left(\frac{\partial^2 w}{\partial r^2}+\frac{1}{r}\frac{\partial w}{\partial z}+\frac{\partial^2 w}{\partial z^2}\right), \tag{2.1c}$$

$$\frac{\partial}{\partial r}(ru)+\frac{\partial}{\partial z}(rw) = 0, \tag{2.1d}$$

where $u$, $v$, $w$ are the velocity components (relative to the rotating cylindrical cavity) in the $r$, $\theta$ and $z$ directions, respectively, and

$$p^1 \equiv p-\tfrac{1}{2}\rho\Omega^2 r^2,$$

where $p$ is the static pressure. In a rotating cavity the nonlinear convection terms in the curly brackets become increasingly less significant at large values of $\Omega$. In fact, for large values of the rotational Reynolds number, $Re_\theta$, and small values of the radial Rossby number, $\epsilon_r$, equations (2.1) can be approximated by

$$-2\Omega v = -\frac{1}{\rho}\frac{\partial p^1}{\partial r}+\nu\frac{\partial^2 u}{\partial z^2}, \tag{2.2a}$$

$$2\Omega u = \nu\frac{\partial^2 v}{\partial z^2}, \tag{2.2b}$$

$$0 = -\frac{1}{\rho}\frac{\partial p}{\partial z}+\nu\frac{\partial^2 w}{\partial z^2}, \tag{2.2c}$$

with the boundary conditions

$$u = v = w = 0 \quad \text{at} \quad z = 0,$$

$$\frac{\partial u}{\partial z} = \frac{\partial v}{\partial z} = \frac{\partial w}{\partial z} = 0 \quad \text{as} \quad z \to \infty,$$

and, for symmetry of the Ekman layers on each disk,

$$\tfrac{1}{2}Q = \int_0^\infty 2\pi r u \, dz.$$

The standard solutions for the Ekman layers are:

$$u = -\bar{v} \exp(-z/D) \sin(z/D), \tag{2.3a}$$

$$v = \bar{v}(1 - \exp(-z/D) \cos(z/D)), \tag{2.3b}$$

$$w = 0, \tag{2.3c}$$

where $\bar{v}$ is the tangential velocity of the inviscid core (between the Ekman layers on the rotating disks of the cylindrical cavity), and

$$\bar{v} = -Q/2\pi rD. \tag{2.4}$$

Equation (2.4) decreases in accuracy with increasing Rossby number, and Faller (1963) has produced a power-series expansion of the nonlinear terms in (2.1) to give the result

$$\bar{v} = -\frac{Q}{2\pi rD}(1 + 0{\cdot}3\epsilon_r + 0{\cdot}388\epsilon_r^2 + \ldots). \tag{2.5}$$

Hide (1968) has obtained approximate solutions of (2.1) to account for the inner layer ((i) in figure 1*b*), where the uniform radial source flow moves into the Ekman layers and the tangential velocity, $v$, is brought to zero at $r = a$, and the outer layer ((iii) in figure 1*b*), where the Ekman layers feed into the uniform sink and the tangential velocity is brought to zero at $r = b$. Hide's estimates of the thickness of the source and sink layers, $\Delta_E$ and $\Delta_K$, respectively, can be expressed as

$$\Delta_E = 3(\tfrac{1}{2}Ds)^{\frac{1}{2}}\{(1 + 1/4X_a^2)^{\frac{1}{2}} + \tfrac{1}{2}X_a\} \tag{2.6a}$$

and

$$\Delta_K = 3(\tfrac{1}{2}Ds)^{\frac{1}{2}}\{(1 + 1/4X_b^2)^{\frac{1}{2}} - \tfrac{1}{2}X_b\}, \tag{2.6b}$$

where

$$X_a = QD^{\frac{1}{2}}/6\sqrt{2}\pi a s^{\frac{1}{2}}\nu \tag{2.6c}$$

and

$$X_b = QD^{\frac{1}{2}}/6\sqrt{2}\pi b s^{\frac{1}{2}}\nu. \tag{2.6d}$$

For large values of $X_a$, (2.6*a*) can be simplified to

$$\Delta_E/a = \epsilon, \tag{2.7}$$

where

$$\epsilon \equiv (r/a)^2 \epsilon_r = Q/4\pi a^2 \Omega D.$$

The above equations for $\Delta_E$ and $\Delta_K$ are only valid for $\Delta_E \ll a$ and $\Delta_K \ll b$.

## 3. Experimental apparatus

The apparatus was similar to that used by Owen & Pincombe (1979), and a schematic arrangement is shown in figure 2.

The rotating cylindrical cavity comprised two Perspex disks of outer radius $b = 190$ mm, and a cylindrical shroud. Each disc was attached at its inner diameter to a stainless-steel tube of inner radius $a = 19$ mm. The axial spacing between the two disks was adjustable but for the tests reported below a gap ratio of $G = 0{\cdot}267$ was used. The whole disk assembly could be rotated at speeds up to 2600 rev./min by a variable-speed electric motor. As the air in the cavity was at virtually atmospheric conditions ($\nu \simeq 1{\cdot}5 \times 10^{-5}$ m$^2$ s$^{-1}$), it was possible to achieve rotational Reynolds numbers up to $Re_\theta \simeq 6{\cdot}5 \times 10^5$. The speed of the electric motor, which was measured to an accuracy of one rev./min by an electronic timer-counter, drifted slowly, but this drift was kept within 1 % during the course of an experiment.

For the radial inlet tests, see figure 1 (*b*), a tubular gauze screen, which rotated with the cavity, was inserted inside the steel tubes at $r = a$. For the axial inlet case, see figure 1 (*a*), no inner gauze tube was inserted, and for both axial and radial inlet tests a perforated shroud was used. This shroud was made from Perspex sheet, 1 mm thickness, with thirty holes of 12·7 mm diameter at 12° angular intervals in the mid-axial plane.

For the axial inlet tests, air was supplied from a calming section, and a 16:1 area-ratio contraction, to the left-hand side of the cavity shown in figure 2. For the radial inlet tests, air could be supplied equally from the left- and right-hand sides. Variable flow rates, to produce a maximum value of $C_w = 4710$ ($Q \simeq 0{\cdot}013$ m$^3$ s$^{-1}$), were obtained from a centrifugal fan, and the flow rate was determined by a calibrated Annubar differential-pressure sensing element. The pressure difference across the 'Annubar' was measured by a micromanometer with a resolution of 0·1 mm w.g. and the flow rate was determined to an accuracy of better than 3 %.

For flow visualization, the air flow was 'seeded' by means of a smoke generator which vaporized large volumes of oil particles (approximately 0·8 $\mu$m diameter). For laser anemometry, a 'micro-fog lubricator' was used to atomize oil particles of approximately 2 $\mu$m diameter. The relationships of Burson, Keng & Orr (1967), for solid-body rotation, indicate that the radial migration error (or ratio of the particle radial velocity to the tangential air velocity) should be less than 0·2 % for the measurements reported below.

For flow visualization, illumination of the cavity was achieved using a 5 mW He–Ne laser and a cylindrical lens to produce slit-illumination in a plane through the axis of rotation (hereafter referred to as 'the $r$, $z$ plane'). For photography, a 2 W argon-ion laser was used for illumination, and an Olympus OM2 camera (operating in the 'aperture preferred' mode) was arranged with the axis of its lens normal to the illuminated plane. With an f 1·8 lens and ASA 1600 film, a minimum exposure time of 1/60 s was necessary.

The laser-doppler anemometer (LDA) comprised transmitting optics (which used a 5 mW He–Ne laser and rotating diffraction grating) and receiving optics arranged in a forward-scatter real-fringe mode. The signal from the photomultiplier in the receiving optics was processed by a Cambridge Consultants tracking filter. The latter produced an analogue voltage proportional to the doppler frequency (which itself was

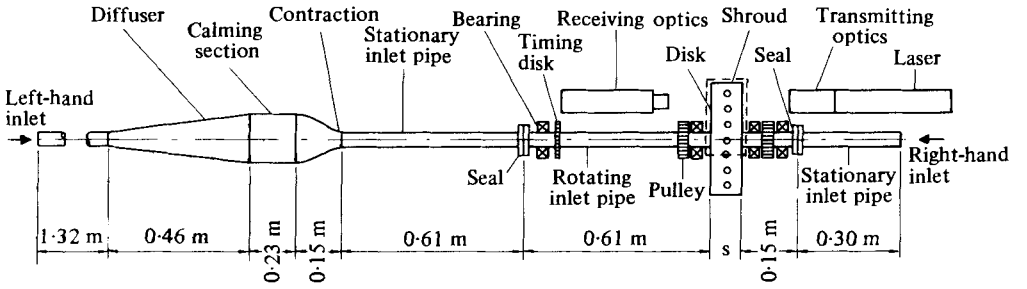


FIGURE 2. Schematic arrangement of the experimantal apparatus. ------, approximate field of view for photographic study.

proportional to the instantaneous component of velocity being measured), and the true time-average was obtained from a digital integrating voltmeter. Further details of the LDA and the accuracy of the velocity measurements can be found in Owen & Pincombe (1979).

## 4. Flow visualization

By illuminating the $r$, $z$ plane and pulsing the smoke generator, it was possible to observe the flow structure inside the rotating cavity. For particular values of flow rate and rotational speed, a sequence of photographs was taken in 'side scatter' (with the axis of the camera lens normal to the plane of illumination) to record the developing smoke patterns that were formed from the time a pulse of smoke entered the cavity until it had been convected to all regions of interest. The field of view for the photographic study is shown in figure 2, but it should be noted that reflexions from each disk gave rise to mirror images at $z = 0$ and $z = s$. It should also be noted that the camera shutter operation was not synchronized with the rotational speed of the cavity.

In order to appreciate the time scale of the photographic sequence, the average outward radial velocity component in the Ekman layers for $0 < z/D < \pi$ takes a time $\tau$ to move from $r = a$ to $r = b$, where from (2.3$a$)

$$\nu b^{-2}\tau = 40 C_w^{-1} Re_\theta^{-\frac{1}{2}}. \tag{4.1}$$

The time that the average inward radial velocity component, for $\pi < z/D < 2\pi$, takes to move from $r = b$ to $r = a$ is approximately $24\tau$.

In §4.1, the overall flow structure is discussed, and details of the inner layer, Ekman layers and outer layer are given in §§4.2–4.4 respectively.

### 4.1. *Overall flow structure*

(*a*) *Radial inlet case.* Figures 3(*a*,*b*,*c*) (plates 1 and 2) show the smoke patterns for $C_w = 79$ (the lowest practicable flow rate) and $Re_\theta = 2{\cdot}5 \times 10^4$ ($\tau = 8$ s) for the case where the flow enters the cavity radially through the fine-mesh cylindrical gauze at $r = a$. Smoke is injected into the upstream flow which enters the centre of the cavity from the left.

Figure 3(*a*) illustrates the flow structure at the time when the smoke has been convected through the inner layer and Ekman layers and has just reached the outer layer, which it leaves via the holes in the perforated shroud. The structure of figure

3(*a*), where the potential core stands out as a black region into which no smoke has penetrated, can be seen to be close to the schematic representation of figure 1(*b*). However, close examination of the Ekman layers in figure 3(*a*) (and in other photographs taken in the same sequence) reveals the existence of a small-amplitude cellular motion with a wavelength an order of magnitude greater than the Ekman-layer thickness.

At these low flow rates, there is evidence of an ingress of fluid from outside the cavity through the holes in the shroud, and smoke that has left the cavity at $r = b$ subsequently re-enters. This inflow creates an additional outer layer (an 'ingress layer') which is an order of magnitude larger than that caused by the outflow (the 'egress layer'). This compound outer layer is visible in figure 3(*b*), and smoke can also be seen to have penetrated the inward-flowing region in the Ekman layers, $\pi < z/D < 2\pi$. This latter effect is clearly visible in figures 3(*c*) where the inward-flowing smoke in the Ekman layers has nearly reached the inner layer. It should be noted that radial inflow in the Ekman layers occurs even when there is no such ingress.

Figure 3(*d*) shows the basic structure for $C_w = 314$ and $Re_\theta = 2{\cdot}5 \times 10^4$, where the flow to the central gauze cylinder was supplied from both sides of the cavity and smoke was injected into the left-hand flow. Comparison of figures 3(*c*) and 3(*d*) reveals that increasing the flow rate has increased the size of the inner layer. Examination of figure 3(*d*) reveals the presence of weak instabilities in the 'developed' Ekman layers adjacent to the potential core and large-scale instabilities in the 'developing' Ekman layers inside the inner layer. These large-scale instabilities give rise to unsteady flow throughout the inner layer. The increase in flow rate has suppressed the ingress of external fluid into the outer layer; however, inflow in the Ekman layers is clearly visible, and smoke from the outer layer has nearly returned to the inner layer.

Figure 3(*e*) shows the structure for $C_w = 628$, $Re_\theta = 2 \times 10^5$, where the low-amplitude long-wavelength cellular patterns in the Ekman layers are supplemented by short-wavelength disturbances. The latter appear to grow from the long-wavelength cells and move axially, in a 'finger-like-fashion', into the potential core. Smoke soon diffuses into the core and the boundaries of the Ekman layers become indistinct, making further flow visualization difficult. These short- and long-wavelength disturbances are discussed in more detail in §4.3.

(*b*) *Axial inlet case.* Figures 3(*f*,*g*) show the smoke patterns for $C_w = 79$ and $Re_\theta = 2{\cdot}5 \times 10$ ($\epsilon_t = 1$) for the case where the flow enters axially from the left and there is no cylindrical gauze at $r = a$ to create a radial source flow. Unlike the radial inlet case (where the central gauze prevents the observations, and perhaps the occurrence, of vortex breakdown) it was found that spiral vortex breakdown occurs for $0{\cdot}3 \leqslant \epsilon_z \leqslant 1$, and evidence of this can be seen by the asymmetric form of the central axial flow. Comparison between figures 3(*f*) and 3(*a*) and between 3(*g*) and 3(*c*) reveals that the main effect of the axial inlet is to alter the structure and size of the inner layer; flow in the Ekman layers and outer layers (including the ingress of external flow) is similar for the axial and radial inlet cases. It should be noted that the axial white band at $r/a \simeq 5$ in figures 3(*f*) and 3(*g*) was caused by reflexion from the shroud and not by smoke penetration. In the radial inlet case, the central gauze prevented such reflexions.

Figure 3(*h*) shows the smoke patterns for the axial inlet case with $C_w = 314$ and $Re_\theta = 2{\cdot}5 \times 10^4$ ($\epsilon_z = 4$). In contrast to the lower flow-rate case, vortex breakdown is absent as is revealed by the axisymmetric form of the central axial flow. Also in

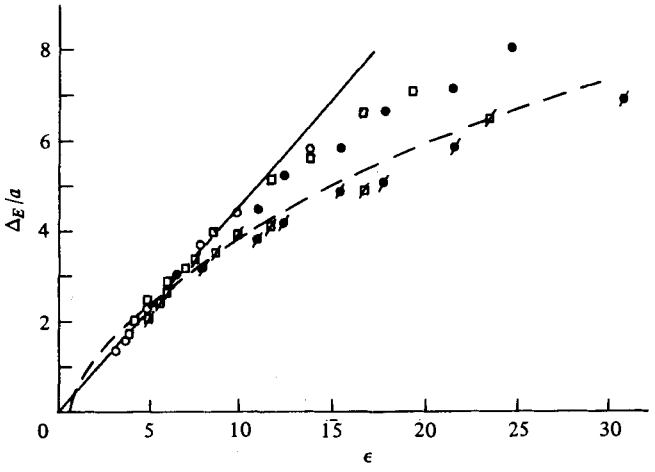


FIGURE 4. The variation of inner-layer thickness with Rossby number, ——, equation (4.2); – –, equation (4.4).

| $C_w$ | 203 | 352 | 643 |
|---|---|---|---|
| Radial inlet | — | ⊠ | ◪ |
| Axial inlet | ○ | □ | ● |

contrast to figure 3 ($f$) (where smoke fills the inner layer before filling the Ekman layer), figure 3 ($h$) reveals that, at this higher flow rate, smoke penetrates into both Ekman layers before it fills the inner layer. It was found that, for the axial inlet case, increasing the flow rate increases the flow into the right-hand side of the inner layer, thereby increasing the circulation (which is anticlockwise in the half of the cavity shown in the photographs). Regardless of the recirculation occurring near the centre of the inner layer, the outer part of this layer distributes the flow equally to the two Ekman layers.

As for the radial-inlet case, Ekman-layer instability occurred for the axial-inlet case and this together with vortex breakdown for $\epsilon_z \leqslant 1$ prevented the observation of steady flow in the inner layer under any condition. Short-wavelength disturbances on the Ekman layers were also observed for the axial-inlet case under similar conditions to those seen on the radial-inlet case.

### 4.2. *The inner layer*

The thickness of the inner layer, $\Delta_E$, was observed to increase with increasing flow rate and decrease with increasing rotational speed. In order to quantify the thickness, the argon-ion laser was used to illuminate the $r, z$ plane, and the He–Ne laser was used to produce an axial beam of light, 0·6 mm diameter, that could be traversed in the radial direction until it coincided with the 'edge' of the smoke-filled inner layer. The error in the measured results was estimated to be approximately 3 mm, and this was attributed to the difficulty in defining an edge to the irregular boundary that (owing to the slow diffusion of smoke) tended to change with time.

Figure 4 shows the measured variation of $\Delta_E/a$ with $\epsilon$ for both the radial and axial inlet cases for a range of flow rates. For large values of $X_a$ (which was the case in the experiments), equation (2.7) suggests that the thickness/Rossby number relation-

ship should be linear, and for $1 < \Delta_E/a < 3$ the experimental results are correlated by

$$\Delta_E/a = 0{\cdot}46\epsilon. \tag{4.2}$$

As these values of $\Delta_E/a$ are outside of the range of Hide's (1968) model, it is surprising that the experimental results agree even qualitatively with his predictions.

In order to explain the behaviour of the inner layer at larger values of $\Delta_E/a$, it is instructive to rewrite equation (2.5) as

$$V_\theta/\Omega r = 1 - 2\epsilon_r(1 + 0{\cdot}3\epsilon_r + 0{\cdot}388\epsilon_r^2 + \ldots), \tag{4.3}$$

where $V_\theta$ is the tangential component of velocity of the potential core relative to a stationary reference frame. From equation (4.3) it follows that $V_\theta$ will equal zero at $\epsilon_r = 0{\cdot}42$, and for larger $\epsilon_r$ (smaller values of $r$) it will become negative. From the velocity measurements discussed in § 5, it would seem that the tangential velocity in the potential core never becomes negative, and the inner layer extends to a point where $V_\theta \simeq 0$, that is $\epsilon_r \simeq 0{\cdot}42$. If we assume that $\Delta_E$ is the thickness of the inner layer to the point where $V_\theta = 0$, it follows from (4.3) that

$$\Delta_E/a = 1{\cdot}5\epsilon^{\frac{1}{2}} - 1. \tag{4.4}$$

It can be seen from figure 4 that (4.4) provides a reasonable approximation for the radial inlet case but tends to underestimate the size of the inner layer for the axial inlet case. This is discussed further in § 5.

### 4.3. *The Ekman layers*

Attempts were made to quantify the critical radial Reynolds number for Ekman-layer instability from visual observation of the smoke patterns in the Ekman layers. For a fixed flow rate and rotational speed, smoke was introduced into the cavity, and the radius at which the 'ripples' in the boundary of the Ekman layers could no longer be discerned with the naked eye was considered to be the critical radius from which $Re_r$ was determined. Measurements were limited to the radial inlet case, where (unlike the asymmetrical axial inlet case) the critical radius was the same in both Ekman layers.

The instability criterion was arbitrary and measurements were subject to large errors (owing to the difficulty in determining when the amplitude of the ripple was negligible). It was found that the critical radial Reynolds number could be correlated by

$$Re_r = 78 - 128\epsilon_r. \tag{4.5}$$

The values of the critical Reynolds numbers estimated from the photographs were consistent with (4.5). However, owing to the limited data and large scatter, the 95% confidence limits in the intercept and slope of equation (4.5) (which was based on eleven data points between $\epsilon_r = 0{\cdot}10$ and $0{\cdot}19$) were 18 and 126, respectively. Tatro & Mollo-Christensen (1967) obtained a correlation for the onset of type II waves for radial inflow (where $\epsilon_r$ is negative) in which

$$Re_r = 56{\cdot}3 - 116{\cdot}8\epsilon_r. \tag{4.6}$$

They also confirmed Faller's (1963) correlation for type I waves where

$$Re_r = 125 - 7{\cdot}32\epsilon_r. \tag{4.7}$$

As the wavelength of the disturbances seen in the present study was consistent with

type II waves ($\lambda/D \simeq 30$), and in view of the similar forms of (4.5) and (4.6), it was concluded that the long-wavelength cellular disturbances were type II waves. According to Tatro & Mollo-Christensen, type I waves do not occur alone, and so the flow visualization techniques used in the present series of tests were not suited to the identification of type I waves.

The short-wavelength disturbances menioned in § 4.1 did not match the description of type I waves (which are confined to the Ekman layers and where $\lambda/D \simeq 12$) but correspond more closely to Tatro & Mollo-Christensen's observations of 'bursts of high frequency fluctuations' that occurred after 'transition to turbulence'. Owing to the rapid diffusion of smoke into the potential core, it was difficult to quantify the precise conditions under which the short-wavelength fluctuations first occurred. From inspection of a number of photographs, these fluctuations were visible when the radial Reynolds number exceeds the value given in (4.5) by between 50 % (at $Re_\theta = 5 \times 10^4$) and 100 % (at $Re_\theta = 2 \times 10^5$). If the presence of the short-wavelength disturbances represent the decay of a structured instability into turbulent flow, then it would seem that increasing the rotational speed delays the transition.

### 4.4. *The outer layer*

Referring to figure 1 (*b*), attempts were made to measure the thickness of the outer layer, $\Delta_K$, for $49 < C_w < 191$, $1{\cdot}1 \times 10^4 < Re_\theta < 2{\cdot}0 \times 10^5$, using the technique described in § 4.2 for measuring $\Delta_E$. As $\Delta_K \ll \Delta_E$, the measurements were prone to large relative errors, and observations were made difficult when the ingress of smoke from outside the cavity occurred. During ingress, as discussed in § 4.1, the structure of the outer layer was complex and its boundary was difficult to define. The only positive statement that can be made about the thickness of the outer layer is that, in the absence of ingress, the order of $\Delta_K$ was that calculated from (2.6).

## 5. Velocity measurements

Detailed measurements of the axial distribution of the radial and tangential components of velocity were made at $r/a = 6{\cdot}00$ and $8{\cdot}33$ for a range of flow rates and rotational speeds. The radial distribution of the tangential velocity in the potential core was measured near the mid-axial plane. For $r/a > 6$, these measurements were made at $z/s = 0{\cdot}5$ with the optics arranged axially; for $r/a < 4$, the measurements were made at $z/s = 0{\cdot}375$ with the optics arranged radially. This departure from the mid-axial plane was necessary to avoid 'flare' from the holes in the shroud. Also, with the optics arranged radially, the presence of the cylindrical gauze tube prevented measurement for the radial inlet case.

In order to compare the measurements, which were made in a stationary reference frame, with the equations of § 2, which were derived for a rotating frame, it is convenient to express (2.3) in terms of $V_\theta$, the tangential component of velocity relative to a stationary frame ($V_\theta = v + \Omega r$), and $U$, the bulk-average radial velocity at $r = a$ ($U = Q/2\pi as$), as

$$\frac{u}{U} = -\frac{\bar{v}}{U} \exp(-z/D) \sin(z/D); \tag{5.1a}$$

$$\frac{V_\theta}{\Omega r} = 1 + \frac{\bar{v}}{\Omega r} (1 - \exp(-z/D) \cos(z/D)). \tag{5.1b}$$

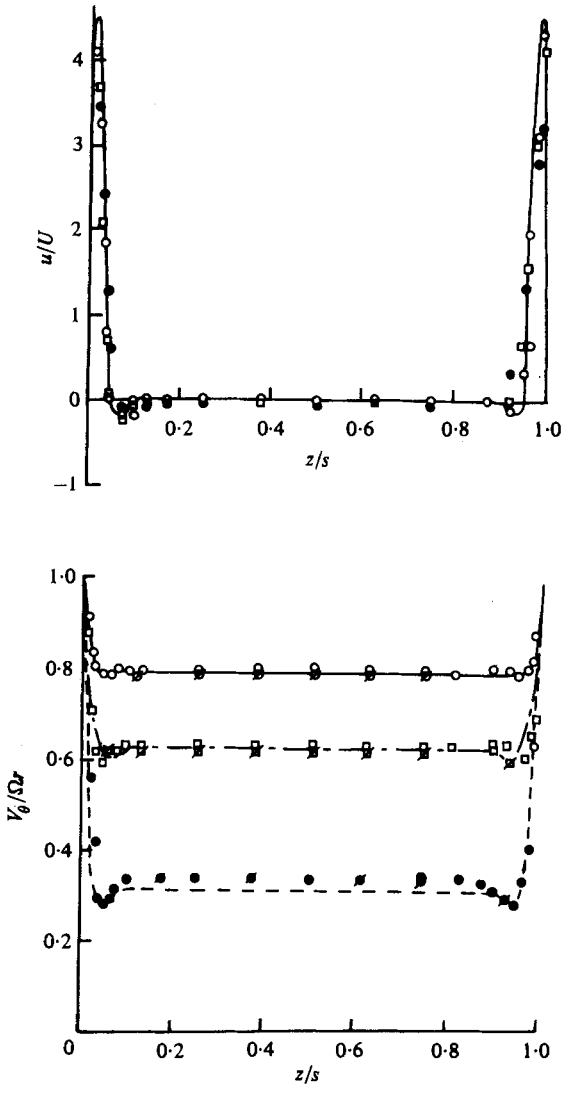


FIGURE 5. The axial distribution of radial and tangential components of velocity at $r/a = 8{\cdot}33$, $Re_\theta = 5 \times 10^4$.

| $\epsilon_r$ | 0·098 | 0·170 | 0·310 | |
|---|---|---|---|---|
| Equation (5.1) | —— | — · — | - - - - - | |
| Axial inlet | ○ | □ | ● | } measured values |
| radial inlet | ⌀ | ⊠ | ◪ | |

For the potential core, (2.4) and (2.5) can be written as

$$\bar{v}/\Omega r = V_\theta/\Omega r - 1 = -2\epsilon_r \tag{5.2}$$

and

$$\bar{v}/\Omega r = V_\theta/\Omega r - 1 = -2\epsilon_r(1 + 0{\cdot}3\epsilon_r + 0{\cdot}388\epsilon_r^2). \tag{5.3}$$

Equation (5.2) being the standard Ekman form and (5.3) being the Faller modification.

Figure 5 shows the axial variation of $u/U$ and $V_\theta/\Omega r$ at $r/a = 8{\cdot}33$ and $Re_\theta = 5 \times 10^4$ for three values of $\epsilon_r$, and compares these with the values obtained from (5.1). It

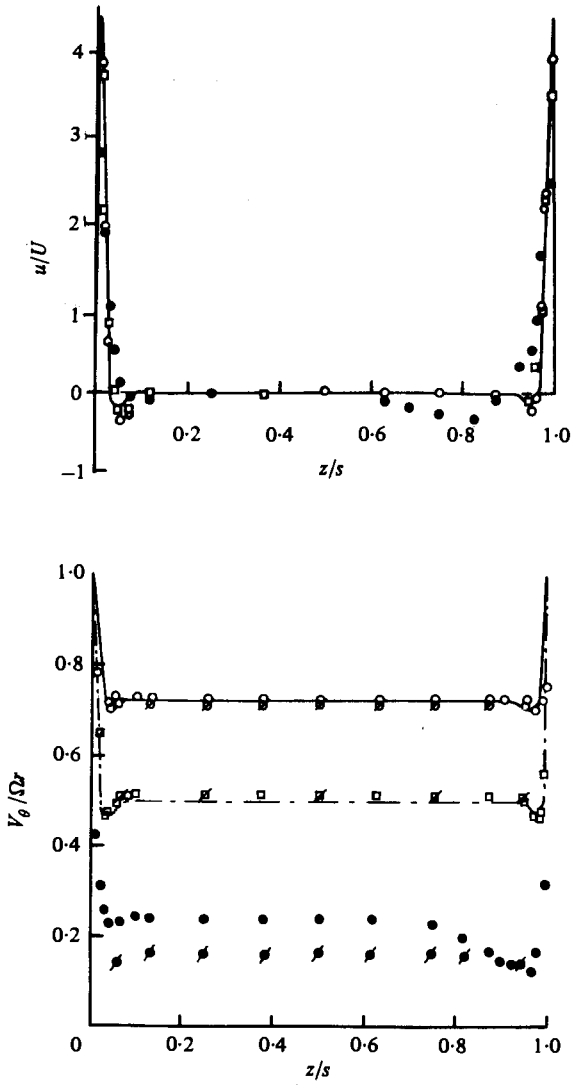


FIGURE 6. The axial distribution of radial and tangential components of velocity at $r/a = 6{\cdot}00$, $Re_\theta = 10^5$.

| $\epsilon_r$ | 0·134 | 0·232 | 0·423 |
|---|---|---|---|
| Equation (5.1) | —— | — · — | |
| Axial inlet | ○ | □ | ● } measured values |
| Radial inlet | ⌀ | ⊠ | ● } measured values |

should be noted that (5.3) was used to calculate $\bar{v}/\Omega r$ in (5.1*b*); the values of $u/U$ calculated from (5.1*a*) are so weakly dependent on $\epsilon_r$ that in figure 5 (and figures 6, 7 and 8) the three theoretical curves for the radial velocity merge into one. The experimental measurements of radial velocity are in good agreement with (5.1*a*), and the reverse flow (which is predicted for $\pi < z/D > 2\pi$, and was discussed in §4) has been measured. The tangential velocity measurements are also in good agreement with (5.1*b*), although there is a small discrepancy at $\epsilon_r = 0{\cdot}310$. This discrepancy may be due to the neglect of higher powers of $\epsilon_r$ in (5.3) or because the Ekman layer in-

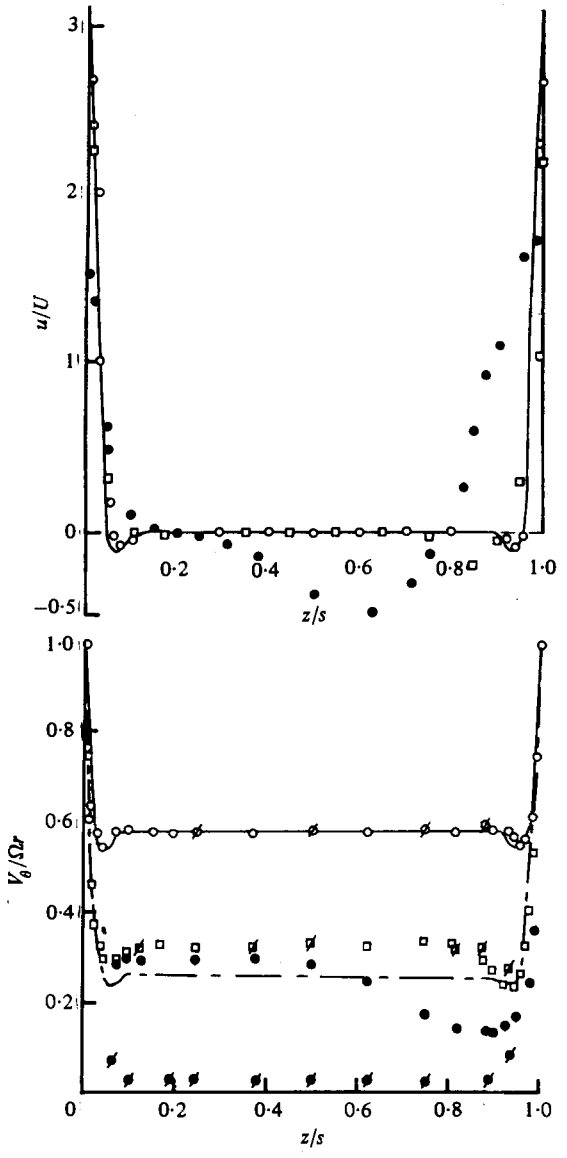


FIGURE 7. The axial distribution of radial and tangential components of velocity at $r/a = 6{\cdot}00$, $Re_\theta = 5 \times 10^4$.

| $\epsilon_r$ | 0·190 | 0·327 | 0·597 |
|---|---|---|---|
| Equation (5.1) | —— | — · — | |
| Axial inlet | ○ | □ | ●, ● } measured values |
| Radial inlet | ⌀ | ⊠ | ● |

stabilities were present. It can also be seen that there is no significant difference between the tangential velocities measured for the axial inlet and the radial inlet cases.

Figure 6 shows similar results for $r/a = 6$ and $Re_\theta = 10^5$. The results for the two lowest Rossby numbers are in good agreement with the theory; at the highest Rossby number

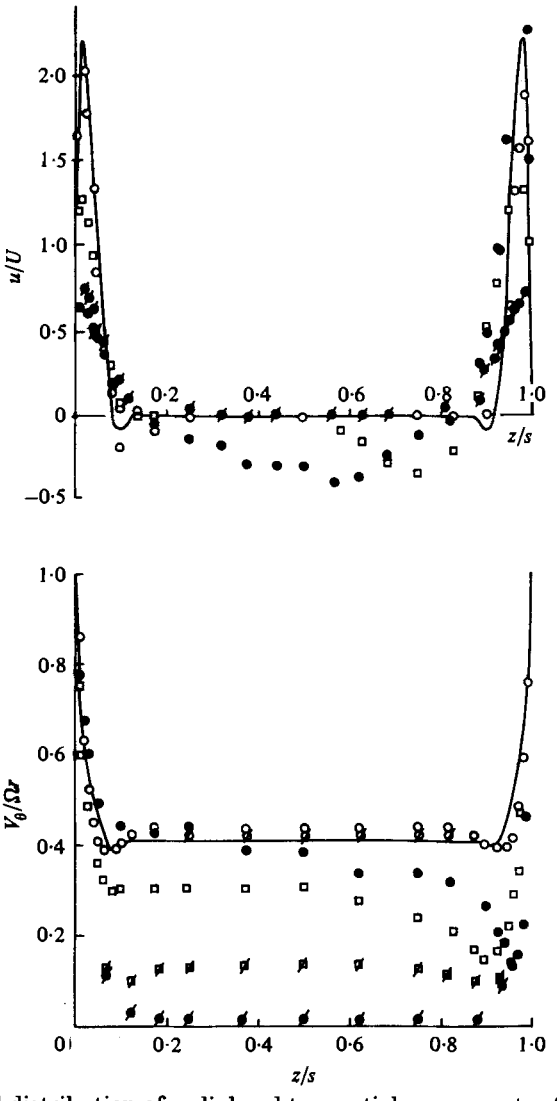


FIGURE 8. The axial distribution of radial and tangential components of velocity at $r/a = 6{\cdot}00$, $Re_\theta = 2{\cdot}5 \times 10^4$.

| $\epsilon_r$ | 0·268 | 0·463 | 0·845 |
|---|---|---|---|
| Equation (5.1) | —— | | |
| Axial inlet | ○ | □ | ●} measured values |
| Radial inlet | ⌀ | ⊠ | ●} measured values |

there is a discrepancy but, at this condition, the inner layer has reached (and for the axial inlet case it has exceeded) $r/a = 6$. For the highest Rossby number, (5.1*b*) and (5.3) predict a negative value for $V_\theta$ (which is not shown in figure 6) in the potential core; in practice, this does not occur, and the actual values of $V_\theta$ exceed those predicted.

Figure 7 shows the results at $r/a = 6$ for $Re_\theta = 5 \times 10^4$. The inner layer extends past this radius for $\epsilon_r = 0{\cdot}597$ (and for $\epsilon_r = 0{\cdot}327$ when the fluid enters the cavity axially), and this can be seen from the measured values of $u/U$, which show that most of the outflow occurs near the downstream (right-hand) disk with a region of inflow between

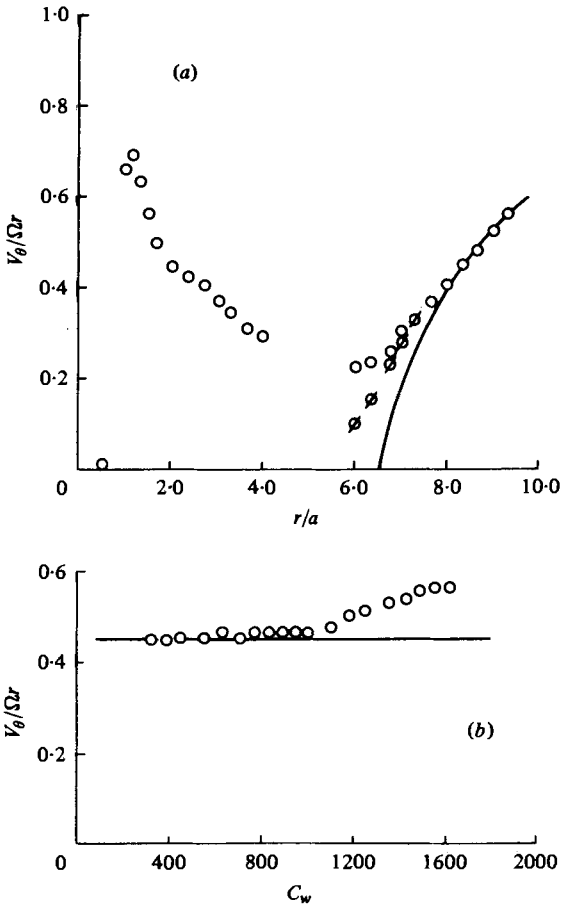


FIGURE 9. Variation of tangential velocity in the mid-axial plane. (*a*) $C_w = 689$, $Re_\theta = 5 \times 10^4$; (*b*) $r/a = 8$, $\epsilon_r = 0{\cdot}25$. ○, axial inlet case; ⌀, radial inlet; ——, equation (5.3).

the disks. The tangential velocity departs from (5.1*b*) for the higher Rossby numbers, and for $\epsilon_r = 0{\cdot}597$ a negative value (which is not shown on the figure) is predicted for $V_\theta$. Not surprisingly, the inlet conditions affect the flow in the inner layer, as can be seen from the measured values of $V_\theta$ at $\epsilon_r = 0{\cdot}597$.

Figure 8 shows a greater influence of the inner layer on measurements made at $r/a = 6$ for $Re_\theta = 2{\cdot}5 \times 10^4$. The inner layer extends past this radius, regardless of inlet conditions, for $\epsilon_r > 0{\cdot}463$, and so (5.1) is only valid for the lowest-Rossby-number case. For the axial inlet case, recirculation inside the inner layer increases with increasing Rossby number (which is equivalent to being 'deeper' inside the inner layer) and the tangential velocity distribution inside the layer depends on the inlet conditions.

Figure 9 shows the behaviour of the tangential velocity inside the potential core. Figure 9 (*a*) shows the variation of $V_\theta/\Omega r$ with $r/a$ for the case of $C_w = 689$ and $Re_\theta = 5 \times 10^4$ ($\epsilon = 24{\cdot}5$). For $r/a < 4$, it was possible to obtain measurements for the axial inlet case only; for $r/a > 6$, the measurements for the radial inlet case are only shown if they depart from the measurements for the axial inlet. Figure 9(*b*) shows the variation of $V_\theta/\Omega r$ with $C_w$ at $r/a = 8$ and $\epsilon = 16$ ($\epsilon_r = 0{\cdot}25$).

It can be seen from figure 9(*a*) that the agreement between the measured and predicted values is good at the larger values of $r/a$. However, at $r/a = 6{\cdot}5$, where (5.3) produces a zero value of $V_\theta$, the measured values have diverged from (5.3). This divergence is attributed to the influence of the inner layer.

For the axial inlet case, the inner layer extends to $r/a = 7$; for the radial inlet case, the layer is smaller. However, for both cases (4.4), which is based on the condition that $V_\theta/\Omega r = 0$ at the edge of the inner layer, provides an approximate estimate of the size of the inner layer. Inside the inner layer, where only measurements for the axial inlet case were possible, it can be seen that $V_\theta/\Omega r$ increases with decreasing radius down to $r = a$ and then falls sharply to zero in a shear layer.

It can be seen from figure 9(*b*) that the measured values of $V_\theta/\Omega r$ in the potential core are in good agreement with (5.3) for $C_w < 1000$ ($Re_r < 200$), but for higher $C_w$ the measured values of $V_\theta$ exceed the theoretical values. Thus, in these radial outflow experiments, where the relative tangential velocity, $\bar{v}$, is negative, the measured values of $\bar{v}$ exceed the theoretical values for $Re_r > 200$. For radial inflow, where $\bar{v}$ is positive, Faller (1963) found that the measured values of $\bar{v}$ become less than the theoretical values for $Re_r > 125$, which was consistent with his observation of type I waves. Although type I waves were not identified in the present series of tests, the short-wavelength fluctuation described in §4.3 would have appeared well before $Re_r = 200$. It is therefore postulated that these short-wavelength disturbances signify the onset of turbulence and that full transition to turbulent flow in the Ekman layers does not occur (under these test conditions) until $Re_r \simeq 200$. It should be pointed out, however, that ingress of external fluid, via the holes in the shroud, occurred for $C_w > 430$ ($Re_r > 86$) in these tests. In order to be more positive about transition from laminar to turbulent flow, it would be necessary to conduct additional experiments on a rig in which such ingress is prevented.

## 6. Conclusions

Flow visualization and laser-doppler anemometry have confirmed that the structure of the flow inside a rotating cylindrical cavity with a radial outflow of fluid is similar to that determined by Hide (1968). In the two cases examined, where the fluid entered either axially or radially near the centre of the cavity and left radially through holes in a peripheral shroud, the structure comprised an inner layer, Ekman layers, an outer layer and an interior potential core. The main difference between the radial and axial inlet cases was in the size and nature of the inner layer.

For the radial inlet case, steady flow was observed in the inner layer at small values of the radial Reynolds number, $Re_r$, but, as $Re_r$ was increased, the flow was readily destabilized by large-scale instabilities generated in the 'developing' Ekman layers. For the axial inlet case, recirculating flow occurred in the inner layer (which tended to be larger than that of the radial inlet case), and the occurrence of Ekman layer instability and/or vortex breakdown in the central jet caused unsteady flow, no matter how small the value of $Re_r$, under all observed conditions.

Measurements of the radial and tangential components of velocity in the Ekman layers were in good agreement with Faller's (1963) 'modified linear theory', and reverse (radially inward) flow, which is predicted to occur in the Ekman layer adjacent to the potential core, was observed and measured. Long-wavelength ($\lambda/D \simeq 30$)

cellular disturbances occurred on the Ekman layers when the radial Reynolds number exceeded a critical value that depended on the radial Rossby number, $\epsilon_r$. The results were correlated by

$$Re_r = 78 - 128\epsilon_r.$$

Short-wavelength 'finger-like' disturbances propagated axially from the long-wavelength cells into the potential core when the critical value of $Re_r$ was exceeded by between 50 % (at low rotational speeds) and 100 % (at high rotational speeds).

Although the thickness of the outer (egress) layer was difficult to quantify, it was an order of magnitude smaller than that of the inner layer and was of order the thickness predicted by Hide. If the flow rate was less than a minimum value, ingress of external fluid occurred through the holes in the peripheral shroud. When ingress occurred the outer layer comprised a thin 'egress layer' for the outflow and a much thicker 'ingress layer' for the inflow of external fluid.

In the potential core, measurement of the tangential component of velocity for $Re_r < 200$ was in good agreement with the modified linear theory. Above this value of radial Reynolds number, the measured velocities exceed the theoretical values. This effect, which occurred well after the appearance of the short-wavelength disturbances, is believed to be associated with transition from laminar to turbulent flow in the Ekman layers.

The authors wish to thank the Science Research Council for sponsoring the work described in this paper and to thank Dr R. H. Rogers for her advice and assistance.

## REFERENCES

Burson, J. H., Keng, E. Y. H. & Orr, C. 1967 Particle dynamics in centrifugal fields. *Powder Tech.* **1**, 305.

Faller, A. J. 1963 An experimental study of the instability of the laminar Ekman boundary layer. *J. Fluid Mech.* **15**, 560.

Hide, R. 1968 On source sink flows in a rotating fluid. *J. Fluid Mech.* **32**, 737.

Owen, J. M. & Bilimoria, E. 1977 Heat transfer in rotating cylindrical cavities. *J. Mech. Engng Sci.* **19**, 175.

Owen, J. M. & Pincombe, J. R. 1979 Vortex breakdown in a rotating cylindrical cavity. *J. Fluid Mech.* **90**, 109.

Tatro, P. R. & Mollo-Christensen, E. L. 1967 Experiments on Ekman layer instability. *J. Fluid Mech.* **28**, 531.

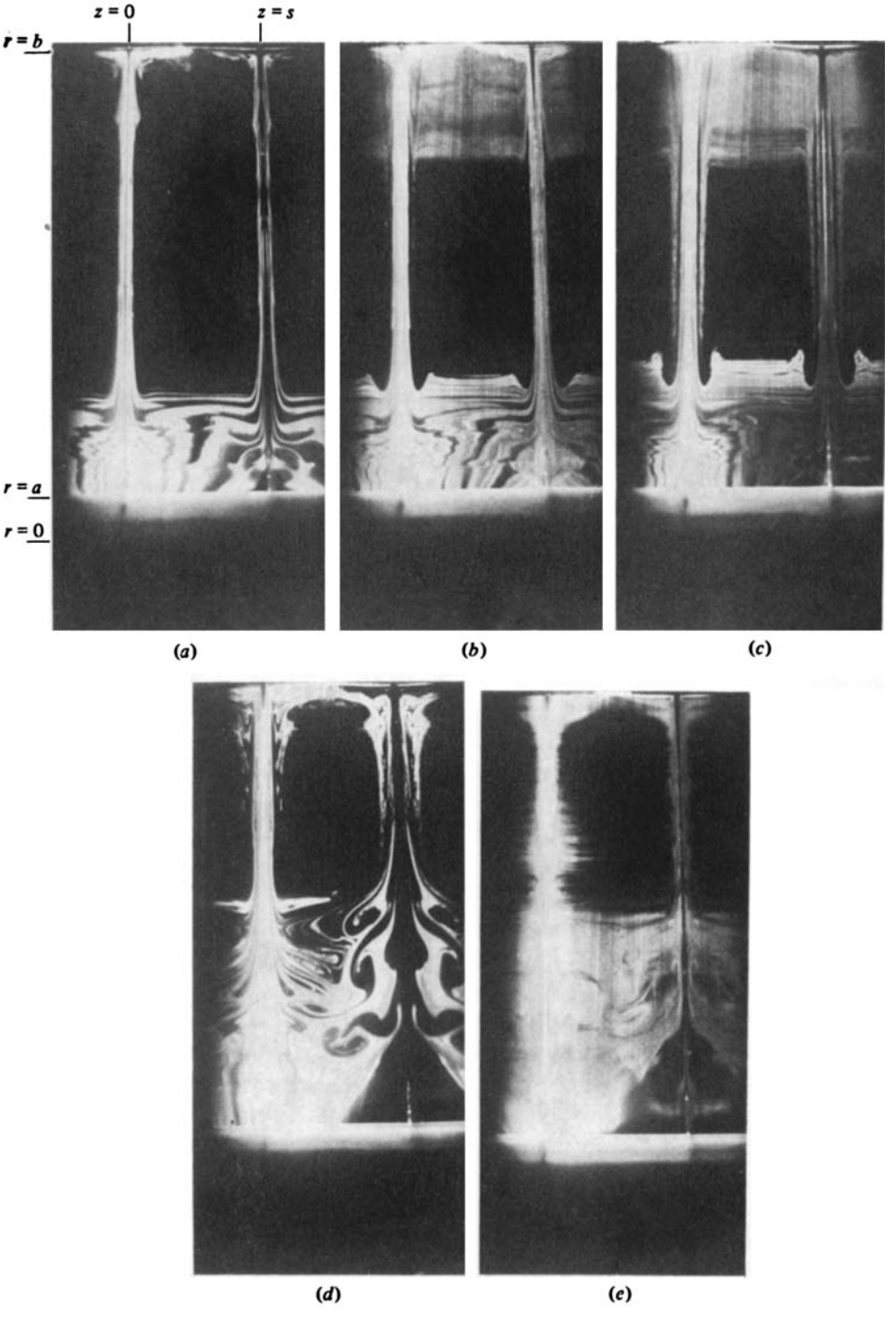


FIGURE 3. For caption to figures (*a*–*e*) see next page.

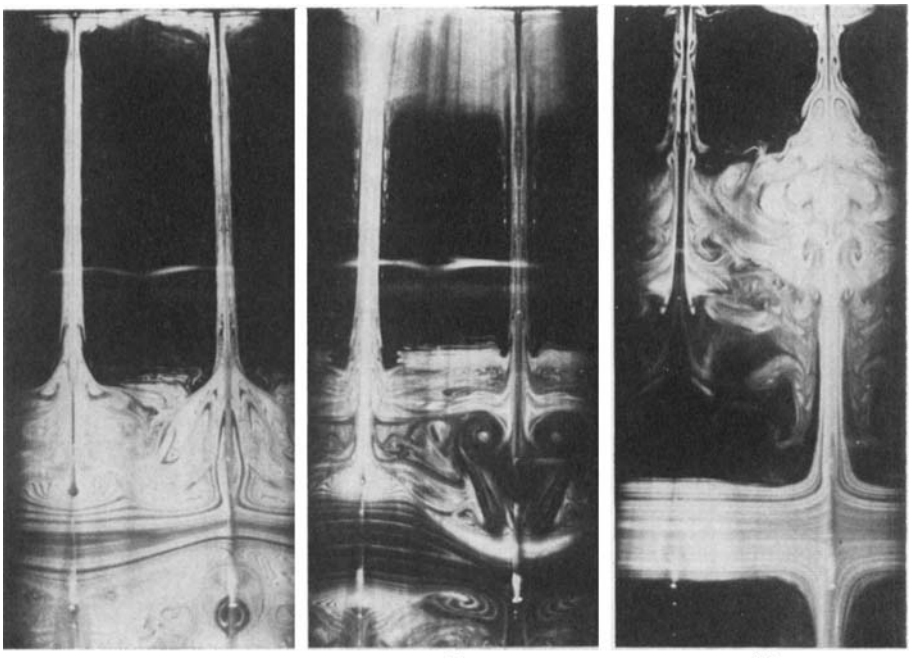

(*f*) (*g*) (*h*)

FIGURE 3. Flow visualization inside the rotating cavity.

Radial inlet: (*a*, *b*, *c*) $C_w = 79$, $Re_\theta = 2{\cdot}5 \times 10^4$; (*d*) $C_w = 314$, $Re_\theta = 2{\cdot}5 \times 10^4$; (*e*) $C_w = 628$, $Re_\theta = 2 \times 10^5$.

Axial inlet: (*f*, *g*) $C_w = 79$, $Re_\theta = 2{\cdot}5 \times 10^4$; (*h*) $C_w = 314$, $Re_\theta = 2{\cdot}5 \times 10^4$.